ACS APPLIED MATERIALS & INTERFACES

Research Article

www.acsami.org

High Performance ZnO-SnO_2:F Nanocomposite Transparent Electrodes for Energy Applications

Gaël Giusti,*[,†] Vincent Consonni,[†] Etienne Puyoo,[†,‡] and Daniel Bellet[†]

[†]Univ. Grenoble Alpes, CNRS-LMGP, F-38000 Grenoble, France

[‡]Institut des Nanotechnologies de Lyon, 7 Avenue Jean Capelle, 69621 Villeurbanne Cedex, France

ABSTRACT: Enhancing the propagation length of light without sacrificing the electro-optical properties of transparent electrodes is of particular interest to solar cells for reaching higher efficiency. This can typically be achieved by nanostructured electrodes but all too often at the expense of complexity and cost-effectiveness. In this work, we demonstrate the simple and low-cost fabrication of a new type of ZnO-SnO_2:F nanocomposite thin film by combining spin-coated ZnO nanoparticles on glass with fluorine-doped SnO_2 thin films deposited by atmospheric spray pyrolysis. The resulting nanocomposites exhibit a dual surface morphology featuring rough ZnO-SnO_2:F nanostructures along with the original smooth SnO_2:F thin film. By readily modulating the surface morphology of ZnO-SnO_2:F nanocomposite thin films with the initial ZnO NP surface coverage, the scattering efficiency of the incident light can remarkably be controlled over the 400−1100 nm solar spectrum wavelength range. High quality hazy ZnO-SnO_2:F thin layers are therefore formed with an averaged haze factor ranging from 0.4 to 64.2% over the 400−1100 nm solar spectrum range while the sheet resistance is kept smaller than 15 Ω/sq for an average total optical transmittance close to 80%, substrate absorption and reflection included. Eventually, optical simulations using Fourier transform techniques are performed for computing the obtained haze factors and show good agreement with experimental data in the 400−1100 nm solar spectrum wavelength range. This opens up additional opportunities for further design optimization of nanoengineered transparent electrodes.

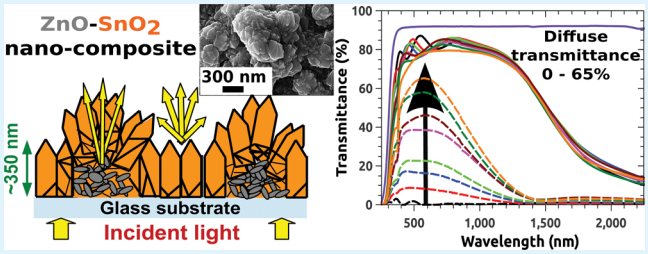

KEYWORDS: *Tin dioxide, ZnO, haze factor, electro-optical, light scattering, nanocomposite transparent electrode*

INTRODUCTION

Transparent conductors (TCs) are an important component of optoelectronic and photovoltaic (PV) devices acting as front transparent electrodes.[1−5] Transparent conducting oxides (TCOs) such as indium tin oxide (ITO), fluorine-doped tin oxide (FTO), or aluminum-doped zinc oxide (AZO) have been so far the materials of choice for manufacturing transparent electrodes.[6,7] As such, they have been extensively studied over the past few decades and there exists a whole industrial ecosystem and know-how around them, both at the laboratory and industry levels. However, this situation is changing driven by search for greater performance materials and cost-efficiency. On the one hand, nanomaterials such as carbon nanotubes,[8] metallic nanowire networks,[9−12] or graphene[13,14] are attracting widespread interest. On the other hand, TCOs are still keeping the upper hand at the industry level but their combination with the previously mentioned nanomaterials to form a nanocomposite could give birth to the "ideal" cost-effective transparent electrode.[15] This nanocomposite concept is extremely promising as recently demonstrated by Kim et al.[16] and Tharsika et et al.,[17] for instance. We are building on these approaches by integrating nanoparticles (NPs) in FTO thin layers with strong emphasis put on the light diffusive power of these transparent electrodes.

The requirements for TCO materials integrated in solar cells are stringent: low electrical sheet resistance (R_s less than 10 Ω/sq) combined with high optical transparency (greater than 90% at 550 nm). In contrast to flat-panel displays, obtaining a large amount of scattered light into the device (and subsequently trapping it) is of particular interest to PV applications such as thin film, organic, dye-sensitized, core−shell nanowire or heterojunction based solar cells to achieve higher photoconversion efficiencies.

Light scattering is the process by which the trajectory of an electromagnetic wave is made to deviate from its initial straightforward path. Such a deviation can stem from diffraction, refraction, reflection, or a combination of these processes. One typically distinguishes surface and volume scattering. Volume scattering takes place at some localized areas of a medium where the refractive index varies. The well-known Rayleigh and Mie scattering are good examples of such phenomena.[18] In contrast, surface scattering occurs at the rough interface between two different media; when its roughness approaches the incident wavelength, light-scattering is particularly efficient. Light is also scattered in reflectance as

Received: June 1, 2014
Accepted: July 30, 2014
Published: July 30, 2014

well as in transmittance, provided the medium is optically transparent. The scattering process is said to be coherent when light is specularly reflected/transmitted; if not, light is said to be diffused and the scattering incoherent, whereupon all phase relationships between scattered wavelets are lost. It is usually considered that light scattered with angles greater than 5° is diffused.

Scattered light enhances the optical path length of photons in solar cells. This increases their probability to be trapped and enventually absorbed, boosting in return the photogenerated current as well as the photoconversion efficiency.[19−21] The advantages are numerous and include reduced material consumption, enhanced collection efficiency, and lower requirements on the absorber layer quality. Along with highly reflective back contacts, surface engineering (introducing periodicity or randomness) of the front electrode can be an efficient and cost-effective way for improving light-scattering and trapping abilities without affecting the overall solar cell architecture. Experimentally, light-scattering efficiency can be assessed by angle-resolved scattering and haze factor measurements. In transmission, the latter is defined as the diffuse over total optical transmittance ratio. These two parameters are strongly impacted by the surface morphology, which strongly depends on the growth methods and/or substrates used.

Atmospheric[22,23] and low-pressure[21,24−26] chemical vapor depositions (CVD), metal organic CVD[27,28] or sputtering[29−31] have been used to grow optimized surface morphologies. For example, random CVD grown ZnO pyramidal-shaped (V-shaped) grains results in surface morphologies demonstrating remarkable light-scattering capabilities.[24,27] Nevertheless, sharp V-shaped grains can have detrimental effects on microcrystalline solar cells by causing cracks necessitating careful optimization of growth conditions for subsequent layer growths;[32] much smoother crater-like morphologies can be obtained by wet-etching and/or plasma treatment. The common issue shared by the previous approaches is related tomorphology limitations inherent to the material itself and growth techniques used. Therefore, in order to achieve greater performance, additional processing on the film surfaces and/or substrates are necessary: wet etching of the thin film surfaces[29,31,33,34] possibly combined with substrate etching,[35] plasma post-treatment,[21] reactive ion etching (RIE),[23,26,28,36,37] nanoimprint lithography,[38,39] or nanomolding.[40] However, this could come at the expense of cost-effectiveness.

Maintaining high optical transparency with a high haze factor and low R_s is not sufficient for solar cell applications: the "ideal" transparent electrode should also combine moderate root-mean-square (RMS) roughness, amenity to high throughput techniques as well as price-competitiveness. So far, large area, high quality, and cost-effective diffuse SnO_2-coated glass substrates are only commercially available from the Asahi glass company (Asahi U-type electrodes).[23] This is the gap we are intending to bridge by demonstrating a versatile low-cost procedure combining a simple ZnO NP spin-coating step followed by atmospheric spray pyrolysis FTO encapsulation. A broad variety of three-dimensional (3D) glass substrates can then be fabricated by varying the surface coverage of ZnO NPs and/or their sizes; let us mention here spray deposition techniques, which are also particularly promising for fabricating large surface area 3D glass substrates.[41,42] It results in a ZnO-SnO_2:F nanocomposite demonstrating superior and controllable light scattering properties competing with the classical random CVD-like pyramidal surface morphology. The crucial interplay between structural and electro-optical properties is discussed as well. Last, but not least, this process is applicable to all types of substrates, NPs, and thin film materials, showing its versatility.

METHODS

Fabrication of the 3D Substrate. ZnO NPs with average diameter of 35 nm were purchased from Sigma-Aldrich. In order to prepare solutions of different mass concentrations (from 0.1 wt % to 2 wt %), different amounts of ZnO NPs were dispersed in isopropyl alcohol. A spin-coater (Spin 150, SPS Europe) was operated to spin-coat these colloidal suspensions on 2.5 × 2.5 cm^2 cleaned alumino-borosilicate glass substrates (Corning glass 1737). A fixed volume of solution (0.4 mL) was spin-coated using a two-stage method (2 × 0.2 mL) while rotational speed (1500 rpm) was maintained constant. The colloidal suspensions were systematically ultrasonicated for 5 min prior to the spin-coating step to break down large aggregates. Eventually, the ImageJ software[43] was used to compute the surface coverage of ZnO aggregates.

Growth of FTO. FTO coating was performed by atmospheric spray pyrolysis as described in ref 44. The aerosol solution was prepared using 0.16 M of $SnCl_4{\cdot}5H_2O$ and 0.04 M of NH_4F in methanol. NH_4F served as the fluorine dopant source. The growth temperature was set to 420 °C and the flow rate was maintained constant at 1.25 mL/min during 20 min, giving thickness of around 350 ± 20 nm with dry air used as carrier gas. A run consisted in nine 2.5 × 2.5 cm^2 Corning glass samples mounted on the heater via a metallic mask so that samples of the same batch (associated with different ZnO surface coverages) were grown under the exact same experimental conditions.

Structural Characterization. The structural morphology of FTO thin films was characterized by field-emission scanning electron microscopy (FESEM) imaging using a ZEISS Ultra+ microscope. The root-mean-square (RMS) roughness of FTO thin films was analyzed by tapping mode atomic force microscopy (AFM) imaging using a Veeco Dimension 3100 microscope after collecting 10 × 10 μm^2 scan size to cover an extended range of spatial frequencies. AFM images comprised 512 × 512 pixels and their postprocessing and analysis were performed using the Gwyddion software.[45] The crystallinity of FTO thin films was investigated by X-ray diffraction (XRD) measurements using a Bruker D8 Advance diffractometer with CuKα_1 radiation (λ = 0.1542 nm) in the Bragg−Brentano configuration (i.e., $\theta/2\theta$ mode). The XRD patterns were all deconvolved from the amorphous peak stemming from the glass substrate and were taken over 2θ = 20−70°. The texture coefficients (C_{hkl}) and the degree of preferred orientation (Σ) were computed from the Harris method by using the following expressions.[46,44]

$$C_{hkl} = \frac{\frac{I_{hkl}}{I_{0,hkl}}}{\frac{1}{N}\sum \frac{I_{hkl}}{I_{0,hkl}}} \quad (1)$$

and

$$\Sigma = \frac{\sqrt{\sum (C_{hkl} - 1)^2}}{\sqrt{N}} \quad (2)$$

where I_{hkl} is the measured X-ray peak intensity of a given plane (hkl) and $I_{0,hkl}$ denotes the standard intensity associated with the plane (hkl) considered from SnO_2 ICDD data [pattern No: 00-041-1445]. Eventually, N represents the number of Bragg diffraction peaks identified in the 2θ angle range of 20 to 70°; in this study, N = 6.

Electro-Optical Characterization. Hall effect measurements were carried out using the Van der Pauw method to determine the sheet resistance (R_s), free carrier concentration (N), and Hall mobility (μ_H). A square array of ohmic contacts arranged on a 2.5 × 2.5 cm^2 sample with a calibrated magnetic field of 0.5 T was used. R_s measurements were also recorded using a linear four-point probe (Lucas Signatone QuadPro, Pro4-440N configuration). The direct (T_D) and total (T_T) optical transmittance spectra were recorded in air by ultraviolet−

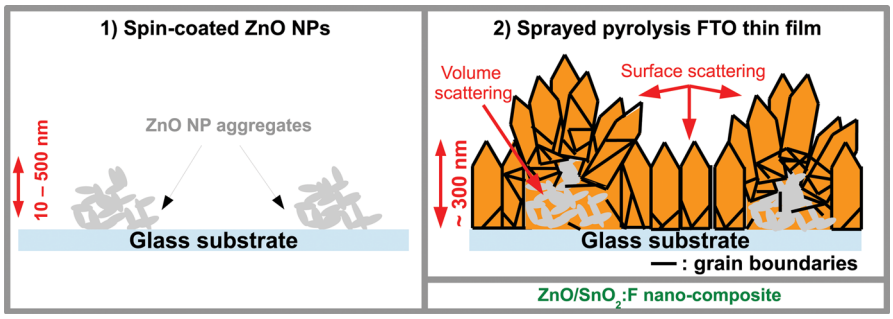

Figure 1. Schematic illustration of the two-step process related to the fabrication of the ZnO-SnO_2:F nanocomposite thin film.

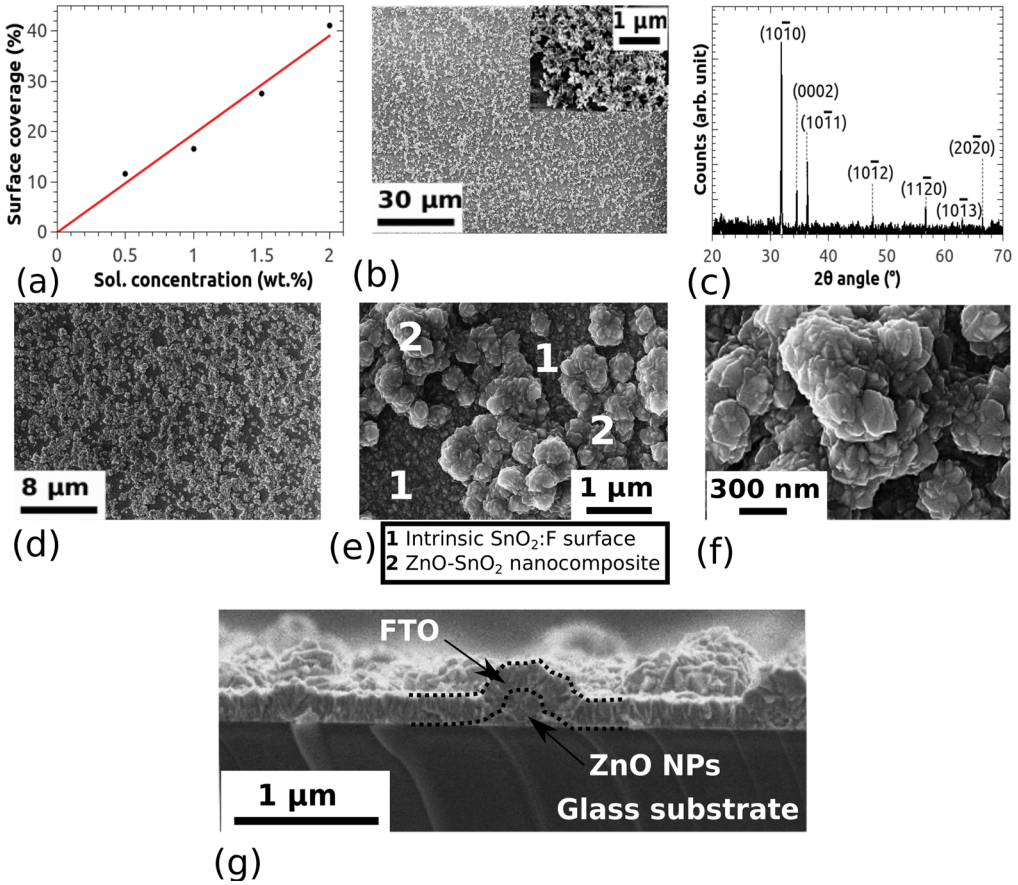

Figure 2. (a) Fitted (red curve) ZnO NP surface coverage versus ZnO NP solution concentration. (b) Low and high (see inset) magnification FESEM images of spin-coated ZnO NPs using a 2 wt % concentrated solution. (c) XRD diffraction pattern of bare spin-coated ZnO NPs on glass. Low (d, e) and high (f) magnification FESEM images of the ZnO-SnO_2:F nanocomposite layers. (g) Cross-sectional FESEM image of the final structure on glass substrate.

visible-near-infrared (UV–Vis–NIR) spectrophotometry using a Lambda 950 PerkinElmer comprising an integrating sphere over the 250 to 2250 nm wavelength range. The transmission spectra background was taken against an air background. The haze factor was calculated by $(T_T - T_D)/T_T = T'_D/T_T$ where T'_D denotes the diffuse transmittance. All the measurements were made at normal incidence and the spot size was around 4 × 10 mm^2.

RESULTS AND DISCUSSION

Architecture. The proposed architecture is schematically presented in Figure 1. A 3D substrate with various characteristic lateral and vertical length scales is first fabricated by a low-cost spin-coating technique using colloidal solutions from commercially available ZnO NPs[47] (step 1). A thin (≈350 ± 20 nm) FTO layer is then grown (step 2) so that the roughness of the randomly distributed and rough ZnO NP aggregates is transferred to the surfaces of the thin FTO layers. As a consequence, a ZnO-SnO_2:F nanocomposite thin film is fabricated, multiplying the number of interfaces and light-scattering centers in volume and from the randomly rough surface. Note that during step 2, samples of the same batch are fabricated under the exact same experimental conditions, thus ensuring meaningful comparisons of their physical properties. Our standard FTO thin layers on flat glass substrate demonstrate state-of-the-art electro-optical properties and pyramidal-shaped grains on the top surface with average grain size of about 100 nm and RMS roughness in the 10–20 nm range.[48,44] Therefore, wavelengths of a few hundred nanometres corresponding to visible light are not efficiently

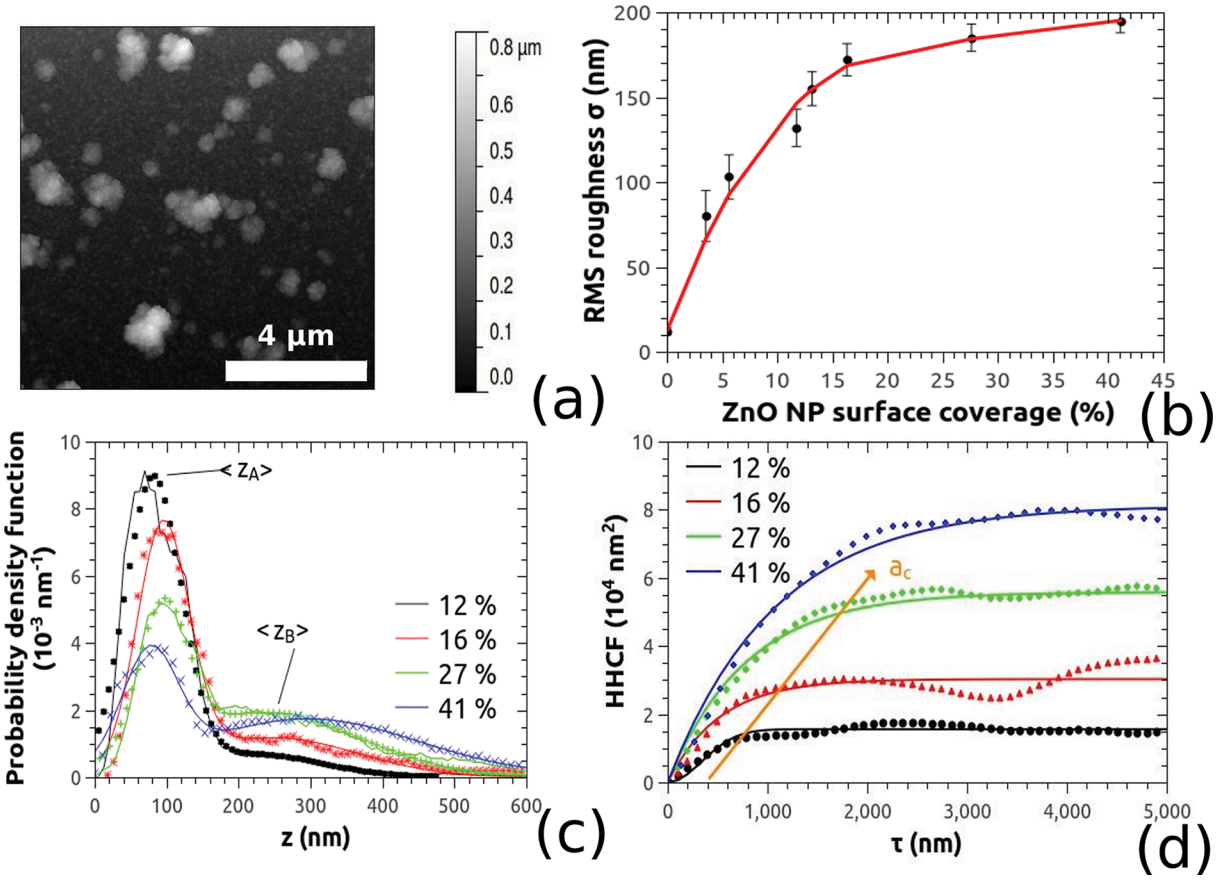

Figure 3. (a) 10 × 10 μm^2 scan AFM image of the rough topographical surface for a surface coverage of 12%. (b) Evolution of the RMS roughness (σ) of ZnO-SnO_2:F nanocomposite layers for various ZnO NP surface coverages. A second-order polynomial fit is used to generate a curve joining experimental points as a guide-to-the-eye. (c) Evolution of the normalized probability density function of the height and (d) HHCF with surface coverage. Dots correspond to the experimental data while straight lines are lines of best fit computed from eq 3. 10 × 10 μm^2 scan sizes are used for the calculations.

diffracted, except in the near-ultraviolet range. Obtaining larger average grain size by growing thicker films would enhance light-scattering but at the expense of optical transmittance and cost-effectiveness. Importantly, this film thickness limitation can be bypassed by using a 3D substrate. In this study, surface scattering at the air/FTO and ZnO/FTO interfaces is solely considered since the difference in the refractive index of FTO ($n \approx 1.80$) and ZnO ($n \approx 1.90$) in the visible range[48] can be neglected to a first approximation. In a word, a nanocomposite thin film is a valuable asset concerning light-scattering enhancement as it promotes light-scattering at interfaces and in volume without modifying much electrical properties, as detailed in the following.

Surface Morphology. The relation between the ZnO NP solution concentration and the corresponding surface coverage is presented in Figure 2a. The different surface coverages are calculated for four concentrations (0.5, 1.0, 1.5, and 2.0 wt %) using the ImageJ software.[43] These calculations are performed over areas as large as 100 × 100 μm^2 in order to be representative as much as possible of the surfaces investigated. As expected, the higher the ZnO NP solution concentration, the higher the surface coverage. Both parameters are linearly correlated in the concentration range investigated. In the rest of this study, surface coverage is extrapolated for concentrations different from 0.5, 1.0, 1.5, and 2.0 wt %.

As observed in Figure 2b, ZnO NPs are not individually found; they consistently form randomly but uniformly distributed 3D ZnO aggregates over the entire substrate area. This point is particularly important for the large surface areas required for solar cell substrates. The high magnification SEM image in inset reveals ellipsoidal shaped ZnO nanocrystallites, which are densely packed into mesoporous micron-scale aggregates. The ZnO NPs are polycrystalline and textured along the $\langle 10\bar{1}0 \rangle$ crystallographic directions (see Figure 2c). The diffraction peaks have all been indexed as hexagonal wurtzite phase of ZnO (ICDD No. 01−075−0576). This texture is consistent with $(10\bar{1}0)$ planes, which exhibit the lowest surface energy in the wurtzite crystalline structure.[49] The agglomeration taking place during the spin-coating step is accounted for by the two following processes: (i) vortex like flows[50] when the fluid spreads over the spinning substrate followed by (ii) evaporation of the volatile ZnO NP dispersion during which attractive interparticle capillary forces likely favor the emergence of self-organized structures.[51,52] The absence of capping agents intensifies attractive Van der Walls forces as well. Lastly, greater shape complexity is demonstrated by ZnO aggregates at higher colloidal ZnO NP concentration since more NP interactions can take place.

After the FTO growth stage, the corresponding low-magnification FESEM image (see Figure 2d) demonstrates a dual surface morphology with good uniformity over a large surface area. The intrinsic SnO_2:F surface is composed of pyramid-like shaped grains with randomly oriented facets and average grain size around 100 nm (see Figure 2e, zone "1");

these are associated with complex-shaped structures resulting from the FTO growth over the underlying ZnO NP aggregates (as shown in Figure 2e, zone "2") whereby the ZnO-SnO_2:F nanocomposite tends to adopt complex shapes similar to roses (see Figure 2f) with numerous sharp edges and tips. Interestingly, this type of rose-like morphology was shown from numerical calculations based on rigorously coupled wave analysis to be particularly efficient as regards light scattering/trapping.[53] The various dimensions of the initial ZnO NP aggregates are concomitant with different structure sizes after FTO coating, typically ranging from a few hundred nanometers to a few microns. Obtaining such a large scale distribution is particularly valuable for light-scattering to take place in the broadest range of the solar spectrum. When FTO is grown over these ZnO NP aggregates, the FTO coating is conformal; moreover, even though ZnO NP aggregates are initially porous, no porosity is evidenced in the final layers (see Figure 2g). This is expected for the CVD technique and from limited self-shadowing effects owing to the coating flux being normal to the translated substrate during the FTO growth step.

Topographical characteristics of the ZnO-SnO_2:F nanocomposite layers examined by AFM are consistent with those previously observed by SEM (see Figure 3a). The RMS roughness (σ) is measured by AFM for different surface coverages, as summarized in Figure 3b and spans a wide range of values from 10 to 200 nm. The surface morphology is further characterized via the plot of the normalized height probability density function (Figure 3c) and the one-dimensional (1D) (along the fast scanning axis x) height−height correlation function (HHCF) (Figure 3d), which are calculated from AFM data using the Gwyddion software.[45] The HHCF is related to the average squared height difference between any two points separated by a given distance. The experimental HHCF data can be fitted with the following expression:[54]

$$\mathrm{HHCF}(x) = 2\sigma^2\left(1 - \exp\left(-\frac{x}{a_c}\right)\right) \quad (3)$$

from which σ and the lateral correlation length a_c can be extracted. a_c represents the average in-plane replication frequency of the roughness profile. As such, it constitutes a valuable complement to σ, which essentially gives "vertical" spatial information. The results of the fit are indicated in Table 1.

Table 1. Fitted Values of the RMS Roughness (σ) and the Surface Lateral Correlation Length (a_c) Using Equation 1 at Four Different Surface Coverages[a]

surface coverage (%)	smooth FTO	12%	16%	27%	41%
σ (nm)	11.6	88. 3	123.1	167.1	210.7
a_c (nm)	43.2	484.4	519.4	785.4	1078.7

[a] σ and a_c are calculated on the basis of 10 × 10 μm^2 AFM pictures with 512 × 512 data points

Basically, a_c increases with surface coverage as the surface morphology demonstrates greater complexity. From Figure 3c, it turns out that the surface can statistically be described as a dual Gaussian surface profile with average heights $\langle z_A \rangle$ and $\langle z_B \rangle$ corresponding to surfaces A and B, respectively. "Surface A" is related to the intrinsic smooth FTO surface while "surface B" corresponds to the ZnO-SnO_2:F nanocomposite. As expected, the higher the surface coverage, the more pronounced the dual height profile as the thin film progressively turns into a nanocomposite material with two distinctive surface morphologies. Interestingly, these can be correlated with the ones obtained by Oyama et al.[23]

Structural Properties. XRD measurements are presented in Figure 4a. The FTO thin films are polycrystalline (six peaks identified) with so-called cassiterite tetragonal crystal phase (ICDD No. 00-041-1445). Only two X-ray diffraction peaks arising from the spin-coated ZnO NPs (ICDD No. 01-075-0576) are discernible at the 27 and 41% surface coverages indicating no potential chemical reaction between ZnO and SnO_2:F (within the X-ray detection limits) during the spray pyrolysis process. Since elastic strain and crystallite size effects could not be properly disentangled, only the Scherrer formula[55] is used to compute the average crystallite size (L_c) for different crystallographic orientations. The crystallite size varies from 15 to 55 nm (see Figure 4b). These values are significantly smaller as compared with the average grain size estimated from FESEM images, which is due to the presence of twins.[44,56] The crystallite size sharply increases for a surface coverage up to a few percents before steadily decreasing (see Figure 4b). To a first approximation, this could be explained by a modified and disordered coalescence stage during Volmer−Weber growth: on the one hand, area with higher nuclei density leading to small crystallite sizes are more likely to show up as compared with a perfectly smooth surface. On the other hand, growth on steep surfaces favors collisions between crystallites, possibly leading to higher local elastic strain as well as twin generation, which is particularly favored in FTO.[57−59] This decrease in average crystallite size with surface coverage is consistent with the degree of preferred orientation (Σ) declining from 0.9 to 0.6 (Figure 4c). This points to a slight structural disordering or randomization taking place with rising surface coverage. This trend is further confirmed by plotting the texture coefficients (C_{hkl}) for the six main peaks previously identified versus surface coverage (Figure 4d): overall, the ZnO-SnO_2:F nanocomposite layers are preferentially oriented along the ⟨100⟩ crystallographic direction regardless of ZnO NP surface coverage, which is in agreement with refs.[44,59−61] However, significant variations are observed for the ⟨110⟩ and ⟨301⟩ directions, highlighting a secondary texture change occurring as surface coverage increases.

Using a thermodynamic approach,[44,59] it is expected that for large elastic strain, strain energy minimization is the driving force for grain growth so that the ⟨100⟩ orientation is predominant. This is supported by experimental results reported in Figure 4d: besides the preponderant ⟨100⟩ orientation, the texture coefficients of the ⟨110⟩ and ⟨301⟩ crystallographic orientations significantly vary. Despite the low elastic biaxial modulus of the ⟨301⟩ orientation, its importance weakens for higher surface coverage. In contrast, the ⟨110⟩ direction increases with surface coverage. Possible increased elastic strain (or increase in defect density) with surface coverage would have suggested the contrary. Clearly, other parameters are to be considered including the dependence of FTO nanocrystal alignments on the substrate surface morphology and nature. Indeed, as surface coverage rises, the FTO nuclei increasingly tend to form and grow on ZnO NP aggregates instead of on glass. Different growth orientations could accordingly be favored owing to the different glass/FTO and ZnO/FTO interface energies. In particular, the ⟨110⟩ direction may be favored on top of ZnO aggregates.

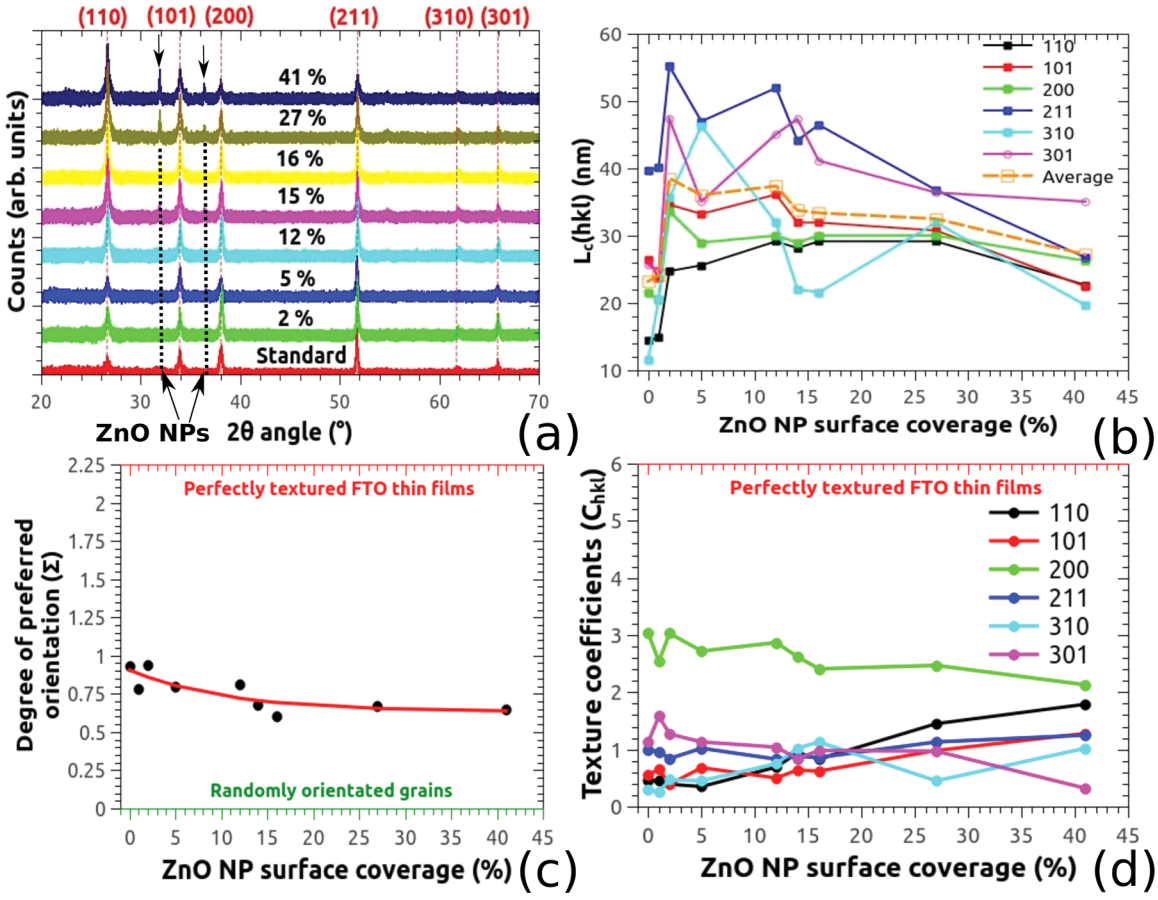

Figure 4. (a) XRD patterns of the ZnO-SnO_2:F nanocomposite layers for different surface coverages. The *h,k,l* indices are associated with the FTO Bragg reflections. X-ray diffraction peaks from the ZnO phase are shown with black arrows. (b) Average crystallite sizes (L_c) for various orientations computed from the Scherrer formula. (c) Degree of preferred orientation (Σ) and (d) texture coefficients (C_{hkl}) versus surface coverage computed from the Harris method.[44,46]

Optical Properties and Simulation. The diffuse and total optical transmittances (T'_D and T_T, respectively) are presented in Figure 5a. T'_D is strongly affected by surface coverage while T_T is almost constant. The shape of T_T spectra is modified with surface coverage: up to 16%, the thin films exhibit prominent interference effects giving birth to oscillations. They are caused by alternatively constructive and destructive interferences between multiple reflections at the smooth air/thin film and thin film/glass interfaces. They gradually disappear for surface coverage higher than about 16% since specular reflectance is less promoted.

In contrast, T'_D can controllably be varied from nearly 0 to 65% in the visible range, which plays a central role in PV. From 600 nm, a pronounced exponential decay in T'_D with increasing wavelength is noticed. It is a common observation for randomly rough surfaces.[20] A decrease of T_T and T'_D for wavelengths below 400 nm is detected owing to the growing bandgap absorption of short-wavelength light in the SnO_2:F layer ($E_g \approx$ 3.7 eV) combined with ZnO NPs ($E_g \approx$ 3.4 eV). Incidentally, such structures could act as back electrodes with their large diffuse reflectance component with the potential to efficiently trap scattered and nonscattered light. A comparison with the Asahi U-type and the recently developed Asahi W-textured electrodes (values taken from ref 23) is provided in Figure 5b. Our nanocomposite thin films clearly compete with such electrodes while being 2 to 3 times thinner and showing similar R_s.

We would now like to draw the attention on the remarkable gradual increase of T'_D. On the one hand, it is accounted for by the reproducible self-organizing process during the spin-coating step: this systematically generates a given surface coverage for a given ZnO NP solution concentration. On the other hand, as these aggregates demonstrate ever more complex shapes, so are FTO structures growing on top of them. As a consequence, the number of sharp edges and corners grow larger, increasing in return light-scattering via diffraction, reflection, refraction on multiple facets and other associated multiple scattering events. Of course, this impacts on σ as well as a_c (see Table 1) which are both similar in magnitude to the incident wavelength. T'_D being directly controlled by σ,[20] larger σ does imply larger T'_D for a given wavelength, as shown by the comparison in between Table 1 and Figure 5a. On a final note, one also cannot rule out an effect of the secondary texture transition from ⟨301⟩ to ⟨110⟩, as evidenced in Figure 4d. It could affect the shape of the grains at the top surface and hence their light-scattering efficiency.

Optical simulations are performed in order to get more insight into the light-scattering behavior of our thin film electrodes from a diffraction standpoint. The scalar diffraction theory offers a theoretical treatment of light-scattering by a surface in which the Kirchhoff and Rayleigh−Sommerfeld formulations are generally adopted.[62] Both often lead to excellent agreement with experimental results. However, the Kirchhoff's boundary conditions were found inconsistent

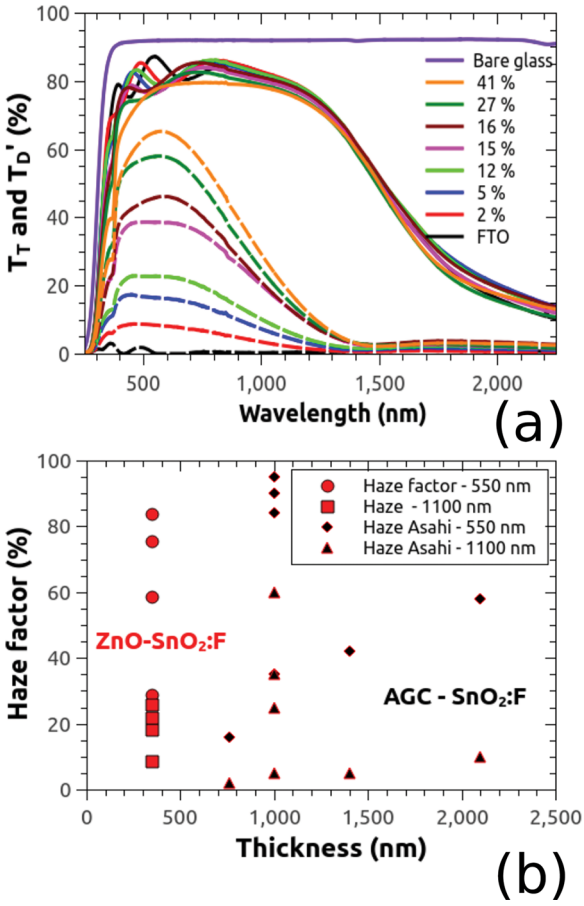

Figure 5. (a) Total (T_T, solid lines) and diffuse (T_D', dashed lines) transmittance spectra of ZnO-SnO_2:F nanocomposite layers over the 250−2250 nm wavelength range versus surface coverage. Note that all the transmittance values include the absorption and reflectance by the glass substrate as well. (b) Haze factors versus film thickness and comparison with data from Asahi glass company (AGC) which develops SnO_2:F electrodes.[23]

contrary to the later formulated Rayleigh−Sommerfeld diffraction theory. In the framework of this theory, Goodman[62] first described light-scattering effects by using Fourier transform techniques. Later on, Harvey[63] generalized Goodman's Fourier treatment and lifted restrictive paraxial approximations for using the scalar scattering theory. He also emphasized that, when dealing with diffraction, the relevant quantity to consider is the diffracted radiance[64] defined as

$$L(\alpha, \beta) = \left(\frac{\lambda^2}{A_s}\right)|F\{U_0(\hat{X}, \hat{Y})\}|^2 \quad (4)$$

where $\alpha = \lambda f_X$ and $\beta = \lambda f_Y$ are the direction cosines of the propagation vectors in the X and Y directions of a Cartesian coordinate system describing a plane in which the aperture (i.e., the illuminated area) lies; f_X and f_Y are the spatial frequencies and λ is the incident wavelength. A_s denotes the surface area under illumination, which is none other than the scanned area size for AFM. The aperture function $U_0(\hat{X},\hat{Y})$ represents the complex amplitude distribution emerging from the aperture, that is, the disturbance undergone by the light wave as it goes through it. F{...} denotes the Fourier transform. Lastly, $\hat{X}$ and $\hat{Y}$ refer to the corresponding distances normalized by the wavelength λ, as suggested in ref 63. $L(\alpha,\beta)$ is expressed in Watts (W) per unit solid angle (steradian or sr.) per unit projected area (m^2).[64]

This approach has recently been further developed and adapted to light-scattering by random rough ZnO surfaces.[65] The authors successfully reproduced angle-resolved and haze factor measurements of their thin films by using the following aperture function $U_0(\hat{X},\hat{Y})$:

$$U_0(\hat{X}, \hat{Y}) = \frac{1}{(1+\varepsilon)^2} e^{i\Delta\varphi} \quad (5)$$

where $\Delta\varphi$ denotes the phase change the light wave experiences as it encounters the rough surface of topography $Z = h(X,Y)$ acting like a random phase grating as presented in Figure 6a. ϵ

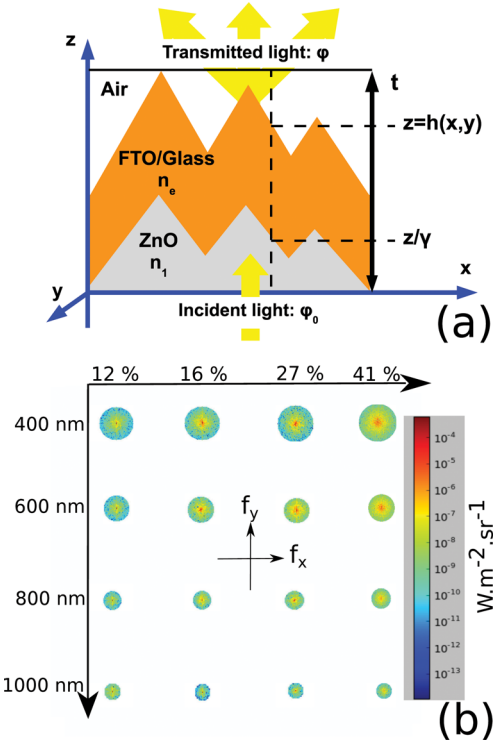

Figure 6. (a) Phase change at normal incidence during propagation through the ZnO-SnO_2:F nanocomposite of thickness t. γ equals 4, 3, and 2 at surface coverages of 12, 16, 27/41%, respectively. φ_0 (φ) refers to the phase of the light as it enters (exits) the nanocomposite. (b) Diffracted radiances ($L(\alpha,\beta)$) (computed from eq 4) of the ZnO-SnO_2:F nanocomposite layers for various surface coverages and wavelengths. All the plots are in the frequency plane (f_X, f_Y).

represents the ratio between the distance from the origin to all points (X,Y) of the aperture and the observation distance. It can be neglected for standard spectrophotometric measurements. The phase change $\Delta\varphi$ requires extra caution when dealing with a nanocomposite thin film; the representation adopted illustrated in Figure 6a is inspired from Dominé et al.[65] It consists of a rough mixed FTO/Glass thin layer of average effective refractive index $n_e = 1.55$ and local topographic height $Z = h(X,Y)$; it is associated with a ZnO thin layer representing the ZnO NPs of average refractive index $n_2 = 1.90$ in the 400−1100 nm wavelength range. To account for the different amounts of NPs incorporated in the nanocomposite, the thickness Z of this ZnO layer is varied through the γ weighting parameter as surface coverage increases from 12% to 41%.

dx.doi.org/10.1021/am5034473 | ACS Appl. Mater. Interfaces 2014, 6, 14096−14107

Eventually, the light exiting the top surface experiences a phase change $\Delta\varphi$:

$$\Delta\varphi = \varphi - \varphi_0 = \frac{2\pi}{\lambda}(n_e - 1)(t - Z) + \frac{2\pi}{\lambda}(n_2 - n_e)\frac{Z}{\gamma} + \frac{2\pi}{\lambda}n_e\left(t - \frac{Z}{\gamma}\right) \quad (6)$$

where φ_0 (φ) is the initial (final) phase of the light wave.

As for the haze factor, it is calculated from

$$H_T = \frac{\sum_{\alpha^2+\beta^2\le 1} L(\alpha, \beta) - L(0, 0)}{\sum_{\alpha^2+\beta^2\le 1} L(\alpha, \beta)} \quad (7)$$

where $L(0,0)$ represents the diffracted radiance corresponding to the specularly scattered light related to the direct optical transmittance. Propagating modes are described by (α,β) where $\alpha^2 + \beta^2 \le 1$; conversely, $\alpha^2 + \beta^2 > 1$ describes evanescent modes. It can be discarded since no significant (localized) surface plasmon polariton coupling is expected. Figure 6b illustrates various diffracted radiances in the frequency plane (f_X, f_Y) as a function of wavelength and surface coverage. The portion shown corresponds to the unit circle in direction cosine space verifying $\alpha^2 + \beta^2 \le 1$ containing propagating modes. Overall, it is appreciated that the greater the surface coverage, the higher the number of high spatial frequency components in the frequency plane (f_X, f_Y). It is consistent with the surface developing greater complexity and finer features coupled with additive random noise presents in the initial AFM image. Lower diffraction efficiency at 1000 nm makes this trend less pronounced. Note the polar geometry of the diffracted radiance suggesting surface isotropy.

The diffracted radiances shown in Figure 6b are obtained after some modifications of the aperture function $U_0(\hat{X},\hat{Y})$ to account for self-shadowing effects. They are introduced via a 2D matrix (shadowing[$\hat{X}$,$\hat{Y}$]) comprising randomly generated 0 and 1. Zero values cancel out any signal getting through the rough surface area and vice versa. By inserting eqs 4, 5, and 6 in eq 7, simulated H_T are calculated and compared with experimental values, as presented in Figure 7.

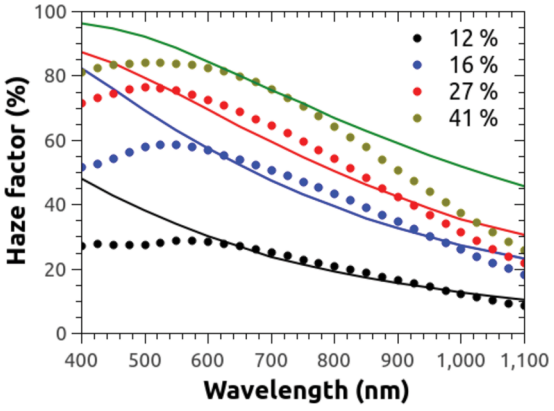

Figure 7. Experimental (points) and simulated (lines) haze factors of ZnO-SnO_2:F nanocomposite layers over the 400−1100 nm wavelength range at four surface coverages. Simulated H_T are computed from eq 7. Note that glass substrate absorption and reflection are included.

The model is in good agreement with experimental data except in the low wavelength range and at the highest surface coverage (41%) where scattering is largely overestimated in both the low and high wavelength ranges. On the experimental side, two main reasons can explain such discrepancies, regardless of surface coverage: (i) the oscillations in the total transmittance spectra (see Figure 5a), particularly at low surface coverage, cannot be taken into account by the model. Yet, they somewhat modify the shape of the spectra and hence the resulting H_T. (ii) As suggested by Bittkau et al.,[66] the better the quality of the AFM images, the better the simulation results of the H_T. Even though, this last point can be handled with very low scan rate when dealing with large aspect ratio surfaces, some detail losses of fine rose-like structures are for instance very difficult to avoid. As for the model limitations, there are two arguments worth mentioning that could explain the overestimation of the H_T in the low and high wavelength ranges. (i) Scattering in volume is not at all accounted for by the model while it is bound to play a larger role in defining the resulting light-scattering properties, particularly at high surface coverage. In the near-infrared range for instance, the agreement is degraded as surface coverage increases: this could be explained by a greater role of Mie scattering since numerous larger aggregates tend to form at high surface coverage. (ii) Sharpe edges and tips (more numerous at high surface coverage) might have a detrimental effect on the prediction of the scattering angle and hence on the light-scattering intensity distribution.[67] Last but not least, let us remember that only diffraction effects are examined. Despite these considerations, the model proves to be predictive within a large portion of the 400−1100 nm wavelength range, especially at low surface coverage in the range of 2 to 16% which is particularly attractive for their integration into solar cells.

Along with the above-mentioned optical properties, one also has to closely track electrical properties: an increasing haze factor should not come at their expense.

Electrical Properties. Hall mobility (μ_H) measurements are performed and the results are summarized in Table 2 along with key optical data. A good agreement is found between R_s values collected from Hall effect according to the Van Der Pauw technique and four-point probe measurements. The carrier concentration remains fairly stable since the FTO depositions was performed under the exact same experimental conditions. However, μ_H does vary to a statistically significant extent. The main scattering mechanisms for charge carriers in polycrystalline FTO thin films are ionized-impurity and grain boundary (including twins) scattering.[56,58] The FTO thin layers are highly doped (degenerated) with carrier concentration of a few 10^{20} cm^{-3} (see Table 2). Hence, the mean free path of free electrons is calculated by

$$l_e = \frac{h}{2e}\left(\frac{3N}{\pi}\right)^{1/3}\mu_H \quad (8)$$

where h is the Planck's constant, e is the elementary charge, N is the free carrier concentration, and μ_H is the Hall mobility. With the values reported in Table 2, $l_e \approx 5.7$ nm. However, the average crystallite and grain substructure sizes estimated from XRD measurements (Figure 4 (b)) are from 15 to 55 nm. This estimation is likely to be much more precise at low rather than at high surface coverage since growth is less impacted by ZnO NP aggregates. (i) At low surface coverage, $l_e \approx 5.7$ nm so that grain boundaries (including twins) scattering is, to a first

Table 2. Summary of the Electro-Optical Properties[a]

concn. (wt %)	SC (%)	R_s (Ω/sq)	ρ (10^{-4} Ω·cm)	N (10^{20} cm^{-3})	μ_H (cm^2/V·s)	avg. T_T (%)	avg. H_T (%)
0	0	9.5	4.0	4.3	36.4 (±2)	82.4	0.4
0.5	12	11.2	4.7	4.3	31.0 (±3)	82.3	19.6
1.0	16	11.9	5.0	3.9	32.1 (±3)	81.4	43.5
1.5	27	11.9	5.0	4.0	31.3 (±3)	79.1	55.5
2.0	41	14.8	6.2	3.5	28.8 (±4)	77.2	64.2

[a] R_s is measured by a 4-point probe. Conc. refers to ZnO NP solution concentrations of the different spin-coated solutions. SC stands for "surface coverage". Hall effect measurements lead to experimental values of electrical resistivity (ρ), carrier concentration N and Hall mobility (μ_H). The experimental total transmittance (T_T) and haze factors (H_T) are averaged over the 400−1100 nm wavelength range. Note that glass substrate absorption and reflection are included

approximation, not the dominant scattering mechanism. In contrast, ionized-impurity scattering is expected to play a major role in determining μ_H, particularly when crystallite sizes get larger as explained in ref 56 for FTO thin films. (ii) At higher surface coverage, where the ZnO/FTO interface no longer play a negligible role, the situation gets more complex: the more aggregates there are, the more complex structures there exist introducing considerable nonuniformity in grain size and presumably in grain-boundary properties such as the barrier height; therefore, at these ZnO/FTO interfaces, scattering taking place at grain boundaries and twins might no longer be insignificant. More importantly, the initially undoped ZnO NPs are not expected to demonstrate good electrical conductivity further impacting on the degradation of lateral mobility. However, the generation of oxygen vacancies (intrinsic doping) during the high temperature stage prior to the FTO growth combined with extrinsic F doping during the growth of FTO could significantly enhance the conductivity of the ZnO NPs. One cannot totally rule out the formation of possibly highly conductive $ZnSnO_3$ and/or Zn_2SnO_4 phases at the ZnO/SnO2:F interface; nevertheless, recent thermodynamic calculations using the ab initio method confirm that at midrange external pressure (<4 GPa) and over the temperature range from 293 to 800 K, the ZnO + SnO_2 phase is the most stable one.[68] Last but not least, no X-ray diffraction peaks corresponding to these phases could be identified pointing out to their quasi-absence and/or to their amorphous nature.

As for the variation in μ_H with surface coverage, they are accounted for by a higher incorporation rate of ionized impurities as a secondary texture transition proceeds with increasing surface coverage (see Figure 4d); this would reinforce the corresponding scattering mechanism and thus lowering μ_H. This incorporation is likely to take place at grain boundaries since the carrier concentration is nearly constant (see Table 2). Incidentally, Wang et al.[69] also pointed out a decrease in μ_H with the increase in the texture coefficient (C_{hkl}) of the ⟨110⟩ direction for SnO_2:F thin films grown by spray pyrolysis, as observed in this work (Figure 4d and Table 2). Moreover, the increasing number and complexity of FTO/ZnO interfaces (at which further scattering can take place) plays in favor of a reduced mobility. All in all, a reduction in μ_H is consistent with increment in ZnO NP surface coverage.

The total optical transmittance T_T of the textured FTO films is also critical for the overall efficiency of the solar cell devices. A low T_T implies that most of the incident light cannot transmit through the film which is of course detrimental to the device efficiency. Tuning H_T while simultaneously maintaining a reasonably high T_T is therefore essential. To illustrate this point, T_T and H_T averaged over the solar spectrum range (400−1100 nm) as well as the corresponding R_s are shown in Figure 8.

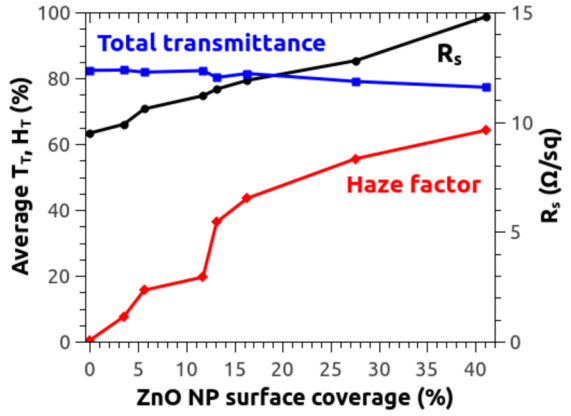

Figure 8. Evolution of T_T (blue curve), H_T (red curve), and R_s (black curve) with surface coverage. Note that glass substrate absorption and reflection are included.

The average T_T (substrate absorption and reflection included) remains high (≈80%) while the average H_T is significantly increased (up to 65%) and the R_s retains values in the 10−15 Ω/sq range. These values are fully compatible with photovoltaic applications and we strongly expect these electrodes to produce a significant increment in photoconversion efficiency of solar cells. For instance, a recent study by Chih-Hung et al.[70] demonstrated an impressive 20% increase in the photoconversion efficiency of dye-sensitized solar cells when using increasingly hazy FTO front transparent electrodes.

CONCLUSIONS

The simple and low-cost fabrication of novel hazy ZnO-SnO_2:F based nanocomposite transparent electrodes is shown by combining spin coated ZnO NPs with SnO_2:F thin films deposited by atmospheric spray-pyrolysis The resulting nanocomposite thin films exhibit a multiscale dual surface morphology involving ZnO-SnO_2:F nanostructures along with the original smooth SnO_2:F thin film. The rough ZnO-SnO_2:F nanostructures are composed of randomly distributed ZnO NP aggregates covered with the SnO_2:F thin film. The original smooth SnO_2:F thin film consists of pyramid-shaped grains with small average grain size, RMS roughness, and lateral correlation length as well as strong preferential orientation. This brings forth complex ZnO-SnO_2:F surface morphologies with a large number of tips, sharp edges and corners, which can

all act as efficient light scattering centers. By readily modulating the total surface coverage of rough ZnO-SnO_2:F nanostructures, the light scattering efficiency of the entire nanocomposite thin films can controllably and reproducibly be adjusted while demonstrating outstanding structural and electro-optical properties that are fully compatible with photovoltaic devices. For moderate RMS roughness (<200 nm) and low average thickness (<350 nm), the average haze factor can be varied from 0.4 to 64.2% in the 400−1100 nm wavelength range while maintaining the total optical transmittance around 80% (glass substrate absorption and reflection included), sheet resistance smaller than 15 Ω/sq, and electron mobility around 30 $cm^2/V·s$. Furthermore, the haze factor is computed by optical simulations using discrete Fourier transform techniques of the experimentally measured surface profile. They show good agreement with experimental data, opening further opportunities in physical property and design optimization of the nanocomposite thin films. Eventually, a huge potential is expected for integrating the present nanocomposite thin films as front transparent electrodes in solar cells for instance.

AUTHOR INFORMATION

Corresponding Author

*Email: gael.giusti@gmail.com.

Notes

The authors declare no competing financial interest.

ACKNOWLEDGMENTS

This work has been supported by the Carnot Institute Energies du Futur under the project ET Nano (contract No. 10B792020A) and by the ANR MetalliGaN (contract No. ANR-12-RMNP-0015-003). The authors thank Xavier Mescot (IMEP-LAHC) for assisting us with the Hall effect measurements. The authors are also grateful to Hervé Roussel for helping with the XRD measurements, Joseph La-Manna for fabricating the metallic mask, and Germain Rey, Carmen Jiménez, Matthieu Jouvert, Daniel Langley, Jérôme Michallon, and Shanting Zhang for their helpful assistance in characterization as well as fruitful discussions.

REFERENCES

(1) Chopra, K. L.; Major, S.; Pandya, D. K. Transparent Conductors—A Status Review. *Thin Solid Films* **1983**, *102*, 1−46.

(2) Gordon, R. G. Criteria for Choosing Transparent Conductors. *Mater. Res. Bull.* **2000**, *25*, 52−57.

(3) Granqvist, C. G. Transparent Conductors as Solar Energy Materials: A Panoramic Review. *Sol. Energy Mater. Sol. Cells* **2007**, *91*, 1529−1598.

(4) Ellmer, K. Past Achievements and Future Challenges in the Development of Optically Transparent Electrodes. *Nat. Photonics* **2012**, *6*, 809−817.

(5) Klein, A. Transparent Conducting Oxides: Electronic Structure−Property Relationship from Photoelectron Spectroscopy with In Situ Sample Preparation. *J. Am. Ceram. Soc.* **2013**, *96*, 331−345.

(6) Ginley, D., Hosono, H., Paine, D., Eds. *Handbook of Transparent Conductors*; Springer Science & Business Media: New York, 2010.

(7) Ellmer, K., Klein, A., Rech, B., Eds. *Transparent Conductive Zinc Oxide: Basics and Application in Thin Film Solar Cells*, 2nd ed.; Springer Verlag: Berlin, Germany, 2008.

(8) Hecht, D. S.; Hu, L.; Irvin, G. Emerging Transparent Electrodes Based on Thin Films of Carbon Nanotubes, Graphene, and Metallic Nanostructures. *Adv. Mater.* **2011**, *23*, 1482−1513.

(9) Lee, J.-Y.; Connor, S. T.; Cui, Y.; Peumans, P. Solution-Processed Metal Nanowire Mesh Transparent Electrodes. *Nano Lett.* **2008**, *8*, 689−692.

(10) De, S.; Higgins, T. M.; Lyons, P. E.; Doherty, E. M.; Nirmalraj, P. N.; Blau, W. J.; Boland, J. J.; Coleman, J. N. Silver Nanowire Networks as Flexible, Transparent, Conducting Films: Extremely High DC to Optical Conductivity Ratios. *ACS Nano* **2009**, *3*, 1767−1774.

(11) Hu, L.; Kim, H. S.; Lee, J. Y.; Peumans, P.; Cui, Y. Scalable Coating and Properties of Transparent, Flexible, Silver Nanowire Electrodes. *ACS Nano* **2010**, *4*, 2955−2963.

(12) Langley, D.; Giusti, G.; Mayousse, C.; Celle, C.; Bellet, D.; Simonato, J.-P. Flexible Transparent Conductive Materials Based on Silver Nanowire Networks: A Review. *Nanotechnology* **2013**, *24*, 452001−20.

(13) Zhao, J.; Pei, S.; Ren, W.; Gao, L.; Cheng, H.-M. Efficient Preparation of Large-Area Graphene Oxide Sheets for Transparent Conductive Films. *ACS Nano* **2010**, *4*, 5245−5252.

(14) Bonaccorso, F.; Sun, Z.; Hasan, T.; Ferrari, A. C. Graphene Photonics and Optoelectronics. *Nat. Photonics* **2010**, *4*, 611−622.

(15) Kumar, A.; Zhou, C. The Race to Replace Tin-Doped Indium Oxide: Which Material Will Win? *ACS Nano* **2010**, *4*, 11−14.

(16) Kim, A.; Won, Y.; Woo, K.; Kim, C.-H.; Moon, J. Highly Transparent Low Resistance ZnO/Ag Nanowire/ZnO Composite Electrode for Thin Film Solar Cells. *ACS Nano* **2013**, *7*, 1081−1091.

(17) Tharsika, T.; Haseeb, A. S. M. A.; Sabri, M. F. M. Structural and Optical Properties of ZnO−SnO_2 Mixed Thin Films Deposited by Spray Pyrolysis. *Thin Solid Films* **2014**, *558*, 283−288.

(18) Hecht, E. *Optics*, 4th ed.; Addison-Wesley Longman, Inc.: Reading, MA, 2002.

(19) Müller, J.; Rech, B.; Springer, J.; Vanecek, M. TCO and Light Trapping in Silicon Thin Film Solar Cells. *Sol. Energy* **2004**, *77*, 917−930.

(20) Zeman, M.; Van Swaaij, R.; Metselaar, J.; Schropp, R. Optical Modeling of a-Si:H Solar Cells with Rough Interfaces: Effect of Back Contact and Interface Roughness. *J. Appl. Phys.* **2000**, *88*, 6436−6443.

(21) Dominé, D.; Buehlmann, P.; Bailat, J.; Billet, A.; Feltrin, A.; Ballif, C. Optical Management in High-Efficiency Thin-Film Silicon Micromorph Solar Cells with a Silicon Oxide Based Intermediate Reflector. *Phys. Status Solidi RRL* **2008**, *2*, 163−165.

(22) Bhachu, D. S.; Waugh, M. R.; Zeissler, K.; Branford, W. R.; Parkin, I. P. Textured Fluorine-Doped Tin Dioxide Films Formed by Chemical Vapour Deposition. *Chem.—Eur. J.* **2011**, *17*, 11613−11621.

(23) Oyama, T.; Kambe, M.; Taneda, N.; Masumo, K. Requirements for TCO Substrate in Si-Based Thin Film Solar Cells-Toward Tandem. *MRS Online Proc. Libr.* **2008**, *1101*, DOI: 10.1557/PROC-1101-KK02-01.

(24) Faÿ, S.; Steinhauser, J.; Oliveira, N.; Vallat-Sauvain, E.; Ballif, C. Opto-Electronic Properties of Rough LP-CVD ZnO:B for Use as TCO in Thin-Film Silicon Solar Cells. *Thin Solid Films* **2007**, *515*, 8558−8561.

(25) Groenen, R.; Löffler, J.; Sommeling, P.; Linden, J.; Hamers, E.; Schropp, R.; van de Sanden, M. Surface Textured ZnO Films for Thin Film Solar Cell Applications by Expanding Thermal Plasma CVD. *Thin Solid Films* **2001**, *392*, 226−230.

(26) Isshiki, M.; Ishikawa, Y.; Ikeda, T.; Oyama, T.; Odaka, H.; Sichanugrist, P.; Konagai, M. SnO_2:F with Very High Haze Value and Transmittance in Near Infrared Wavelength for Use as Front Transparent Conductive Oxide Films in Thin-Film Silicon Solar Cells. *MRS Online Proc. Libr.* **2013**, *1536*, 63−69.

(27) Wenas, W. W.; Yamada, A.; Konagai, M.; Takahashi, K. Textured ZnO Thin Films for Solar Cells Grown by Metalorganic Chemical Vapor Deposition. *Jpn. J. Appl. Phys.* **1991**, *30*, L441−L443.

(28) Hongsingthong, A.; Krajangsang, T.; Yunaz, I. A.; Miyajima, S.; Konagai, M. ZnO Films with Very High Haze Value for Use as Front Transparent Conductive Oxide Films in Thin-Film Silicon Solar Cells. *Appl. Phys. Express* **2010**, *3*, 051102−3.

(29) Guillén, C.; Montero, J.; Herrero, J. Transparent and Conductive Electrodes Combining AZO and ATO Thin Films for

Enhanced Light Scattering and Electrical Performance. *Appl. Surf. Sci.* **2013**, *264*, 448−452.
(30) Wang, Y.; Zhang, X.; Bai, L.; Huang, Q.; Wei, C.; Zhao, Y. Effective Light Trapping in Thin Film Silicon Solar Cells from Textured Al Doped ZnO Substrates with Broad Surface Feature Distributions. *Appl. Phys. Lett.* **2012**, *100*, 263508−4.
(31) Yen, W.; Lin, Y.; Ke, J. Surface Textured ZnO:Al Thin Films by Pulsed DC Magnetron Sputtering for Thin Film Solar Cells Applications. *Appl. Surf. Sci.* **2010**, *257*, 960−968.
(32) Python, M.; Dominé, D.; Söderström, T.; Meillaud, F.; Ballif, C. Microcrystalline Silicon Solar Cells: Effect of Substrate Temperature on Cracks and Their Role in Post-Oxidation. *Progr. Photovoltaics* **2010**, *18*, 491−499.
(33) Nasuno, Y.; Kohama, N.; Nishimura, K.; Hayakawa, T.; Taniguchi, H.; Shimizu, M. Effect of Perforated Transparent Electrodes on Light Transmittance and Light Scattering in Substrates used for Microcrystalline Silicon Thin-Film Solar Cells. *Appl. Phys. Lett.* **2006**, *88*, 071909−4.
(34) Owen, J. I.; Hüpkes, J.; Zhu, H.; Bunte, E.; Pust, S. E. Novel Etch Process to Tune Crater Size on Magnetron Sputtered ZnO:Al. *Phys. Status Solidi A* **2011**, *208*, 109−113.
(35) Isabella, O.; Krč, J.; Zeman, M. Modulated Surface Textures for Enhanced Light Trapping in Thin-Film Silicon Solar Cells. *Appl. Phys. Lett.* **2010**, *97*, 101106−3.
(36) Song, Y. M.; Park, G. C.; Kang, E. K.; Yeo, C. I.; Lee, Y. T. Antireflective Grassy Surface on Glass Substrates with Self-Masked Dry Etching. *Nanoscale Res. Lett.* **2013**, *8*, 1−5.
(37) Hussain, S. Q.; Ahn, S.; Park, H.; Kwon, G.; Raja, J.; Lee, Y.; Balaji, N.; Kim, H.; Le, A. H. T.; Yi, J. Light Trapping Scheme of ICP-RIE Glass Texturing by SF6/Ar Plasma for High Haze Ratio. *Vacuum* **2013**, *94*, 87−91.
(38) Battaglia, C.; Escarré, J.; Söderström, K.; Erni, L.; Ding, L.; Bugnon, G.; Billet, A.; Boccard, M.; Barraud, L.; De Wolf, S.; Haug, F.-J.; Despeisse, M.; Ballif, C. Nanoimprint Lithography for High-Efficiency Thin-Film Silicon Solar Cells. *Nano Lett.* **2011**, *11*, 661−665.
(39) Wang, F.; Subbaiyan, N. K.; Wang, Q.; Rochford, C.; Xu, G.; Lu, R.; Elliot, A.; D'Souza, F.; Hui, R.; Wu, J. Development of Nanopatterned Fluorine-Doped Tin Oxide Electrodes for Dye-Sensitized Solar Cells with Improved Light Trapping. *ACS Appl. Mater. Interfaces* **2012**, *4*, 1565−1572.
(40) Battaglia, C.; Escarré, J.; Söderström, K.; Charrière, M.; Despeisse, M.; Haug, F.-J.; Ballif, C. Nanomoulding of Transparent Zinc Oxide Electrodes for Efficient Light Trapping in Solar Cells. *Nat. Photonics* **2011**, *5*, 535−538.
(41) Sarkar, K.; Braden, E. V.; Pogorzalek, S.; Yu, S.; Roth, S. V.; Müller-Buschbaum, P. Monitoring Structural Dynamics of In situ Spray-Deposited Zinc Oxide Films for Application in Dye-Sensitized Solar Cells. *ChemSusChem* **2014**, DOI: 10.1002/cssc.201402049.
(42) Lehraki, N.; Aida, M. S.; Abed, S.; Attaf, N.; Attaf, A.; Poulain, M. ZnO Thin Films Deposition by Spray Pyrolysis: Influence of Precursor Solution Properties. *Curr. Appl. Phys.* **2012**, *12*, 1283−1287.
(43) Image Processing and Analysis. http://rsbweb.nih.gov/ij/ (accessed Feb. 12, 2014).
(44) Consonni, V.; Rey, G.; Roussel, H.; Bellet, D. Thickness Effects on the Texture Development of Fluorine-Doped SnO_2 Thin Films: the Role of Surface and Strain Energy. *J. Appl. Phys.* **2012**, *111*, 033523−7.
(45) Gwyddion Program. http://gwyddion.net/ (accessed Jan. 30, 2014).
(46) Harris, G. X. Quantitative Measurement of Preferred Orientation in Rolled Uranium Bars. *Philos. Mag.* **1952**, *43*, 113−123.
(47) Zinc Oxide Nanopowder. http://www.sigmaaldrich.com/catalog/product/aldrich/544906?lang=fr_regi (accessed March 4, 2014).
(48) Rey, G. Etude d'Oxydes Métalliques Nano-structurés (ZnO, SnO_2) pour Applications Photovoltaïques. Ph.D. thesis, University of Grenoble, France, 2012.
(49) Wander, A.; Schedin, F.; Steadman, P.; Norris, A.; McGrath, R.; Turner, T. S.; Thornton, G.; Harrison, N. M. Stability of Polar Oxide Surfaces. *Phys. Rev. Lett.* **2001**, *86*, 3811−3814.
(50) Wahal, S.; Oztekin, A.; Bornside, D. E.; Brown, R. A.; Seidel, P. K.; Ackmann, P. W.; Geyling, F. T. Visualization of a Gas Flow Instability in Spin Coating Systems. *Appl. Phys. Lett.* **1993**, *62*, 2584−2586.
(51) Lawrence, C. J. The Mechanics of Spin Coating of Polymer Films. *Phys. Fluids* **1988**, *31*, 2786−2795.
(52) Kralchevsky, P. A.; Denkov, N. D. Capillary Forces and Structuring in Layers of Colloid Particles. *Curr. Opin. Colloid Interface Sci.* **2001**, *6*, 383−401.
(53) Gjessing, J.; Sudbø, A.; Marstein, E. Comparison of Periodic Light-Trapping Structures in Thin Crystalline Silicon Solar Cells. *J. Appl. Phys.* **2011**, *110*, 033104−8.
(54) Sinha, S. K.; Sirota, E. B.; Garoff, S.; Stanley, H. B. X-ray and Neutron Scattering from Rough Surfaces. *Phys. Rev. B* **1988**, *38*, 2297−2311.
(55) Bellet, D.; Bellet-Amalric, E. In *Physical Characterisation of Photovoltaic Materials*; Conibeer, G., Willoughby, A., Eds.; John Wiley & Sons, Ltd: Chichester, U.K., 2014; Chapter 3, pp 35−63.
(56) Rey, G.; Ternon, C.; Modreanu, M.; Mescot, X.; Consonni, V.; Bellet, D. Electron Scattering Mechanisms in Fluorine-Doped SnO_2 Thin Films. *J. Appl. Phys.* **2013**, *114*, 183713−9.
(57) Bruneaux, J.; Cachet, H.; Froment, M.; Messad, A. Correlation between Structural and Electrical Properties of Sprayed Tin Oxide Films with and without Fluorine Doping. *Thin Solid Films* **1991**, *197*, 129−142.
(58) Messad, A.; Bruneaux, J.; Cachet, H.; Froment, M. Analysis of the Effects of Substrate Temperature, Concentration of Tin Chloride and Nature of Dopants on the Structural and Electrical Properties of Sprayed SnO_2 Films. *J. Mater. Sci.* **1994**, *29*, 5095−5103.
(59) Consonni, V.; Rey, G.; Roussel, H.; Doisneau, B.; Blanquet, E.; Bellet, D. Preferential Orientation of Fluorine-Doped SnO_2 Thin Films: The Effects of Growth Temperature. *Acta. Mater.* **2013**, *61*, 22−31.
(60) Agashe, C.; Marathe, B. R. Influence of Film Thickness and Substrate on the Growth of Sprayed SnO_2:F Films. *J. Phys. D: Appl. Phys.* **1993**, *26*, 2049−2054.
(61) Smith, A.; Laurent, J. M.; Smith, D. S.; Bonnet, J. P.; Clemente, R. R. Relation between Solution Chemistry and Morphology of SnO_2-based Thin Films Deposited by a Pyrosol Process. *Thin Solid Films* **1995**, *266*, 20−30.
(62) Goodman, J. *Introduction to Fourier Optics*, 2nd ed.; McGraw-Hill Book Company: New York, 1996.
(63) Harvey, J. E. Fourier Treatment of Near-Field Scalar Diffraction Theory. *Am. J. Phys.* **1979**, *47*, 974−980.
(64) Harvey, J. E.; Vernold, C. L.; Krywonos, A.; Thompson, P. L. Diffracted Radiance: A Fundamental Quantity in Nonparaxial Scalar Diffraction Theory. *Appl. Opt.* **1999**, *38*, 6469−6481.
(65) Dominé, D.; Haug, F.-J.; Battaglia, C.; Ballif, C. Modeling of Light Scattering from Micro- and Nanotextured Surfaces. *J. Appl. Phys.* **2010**, *107*, 044504−8.
(66) Bittkau, K.; Schulte, M.; Klein, M.; Beckers, T.; Carius, R. Modeling of Light Scattering Properties from Surface Profile in Thin-Film Solar Cells by Fourier Transform Techniques. *Thin Solid Films* **2011**, *519*, 6538−6543.
(67) Dominé, D. The Role of Front Electrodes and Intermediate Reflectors in the Optoelectronic Properties of High-Efficiency Micromorph Solar Cells. Ph.D. thesis, University of Neuchâtel, Switzerland, 2009.
(68) Lee, J.; Lee, S.-C.; Hwang, C. S.; Choi, J.-H. Thermodynamic Stability of Various Phases of Zinc Tin Oxides From Ab Initio Calculations. *J. Mater. Chem. C* **2013**, *1*, 6364−6374.
(69) Wang, J. T.; Shi, X. L.; Liu, W. W.; Zhong, X. H.; Wang, J. N.; Pyrah, L.; Sanderson, K. D.; Ramsey, P. M.; Hirata, M.; Tsuri, K. Influence of Preferred Orientation on the Electrical Conductivity of Fluorine-Doped Tin Oxide Films. *Sci. Rep.* **2014**, *4*.

(70) Chih-Hung, T.; Sui-Ying, H.; Tsung-Wei, H.; Yu-Tang, T.; Yan-Fang, C.; Jhang, Y. H.; Hsieh, L.; Chung-Chih, W.; Yen-Shan, C.; Chieh-Wei, C.; Chung-Chun, L. Influences of Textures in Fluorine-Doped Tin Oxide on Characteristics of Dye-Sensitized Solar Cells. *Org. Electron.* **2011**, *12*, 2003−2011.